JOURNAL OF APPLIED PHYSICS **115**, 214504 (2014)

Simulation of thermal reset transitions in resistive switching memories including quantum effects

M. A. Villena,[1] M. B. González,[2] F. Jiménez-Molinos,[1] F. Campabadal,[2] J. B. Roldán,[1] J. Suñé,[3] E. Romera,[4] and E. Miranda[3]
[1]*Departamento de Electrónica y Tecnología de Computadores, Universidad de Granada, Facultad de Ciencias, Avd. Fuentenueva s/n, 18071 Granada, Spain*
[2]*Institut de Microelectrònica de Barcelona, IMB-CNM (CSIC), Campus UAB, 08193 Bellaterra, Spain*
[3]*Departament d'Enginyeria Electrònica, Universitat Autònoma de Barcelona, Bellaterra Cerdanyola del Vallès 08193, Spain*
[4]*Departamento de Física Atómica, Molecular y Nuclear and Instituto Carlos I de Física Teórica y Computacional, Universidad de Granada, Avd. Fuentenueva s/n, 18071 Granada, Spain*

(Received 9 April 2014; accepted 22 May 2014; published online 4 June 2014)

An in-depth study of reset processes in RRAMs (Resistive Random Access Memories) based on $Ni/HfO_2/Si\text{-}n^+$ structures has been performed. To do so, we have developed a physically based simulator where both ohmic and tunneling based conduction regimes are considered along with the thermal description of the devices. The devices under study have been successfully fabricated and measured. The experimental data are correctly reproduced with the simulator for devices with a single conductive filament as well as for devices including several conductive filaments. The contribution of each conduction regime has been explained as well as the operation regimes where these ohmic and tunneling conduction processes dominate. © *2014 AIP Publishing LLC*. [http://dx.doi.org/10.1063/1.4881500]

I. INTRODUCTION

Non-volatile memories based on the resistive switching effects (known as Resistive Random Access Memories, RRAMs) are currently under scrutiny in the scientific community because of their potential to solve the limitations of the conventional flash technology.[1–3] RRAMs show many interesting features in comparison with flash memories and other current proposals in the non-volatile memory realm; among them we could highlight the following: a low program/erase current, fast speed, nano-scale operation characteristics, endurance and viability for 3D memory stacks, and CMOS technology compatibility.[1,4]

RRAMs can be fabricated with metal oxides; in this case, the devices usually show different resistance states produced by the alternating formation and rupture of one or several conductive filaments (CFs).[3,5–8] After a forming process on pristine devices, a low resistance state (LRS) is achieved; it can be switched to a high resistance state (HRS) by the partial dissolution of the CFs (reset) and the HRS can be turned back again to the LRS through a set process that reforms the CFs. Recently, an analysis (comparing experimental and simulation results) of the physics behind thermally assisted reset processes has been published in Refs. 9 and 10; other authors have also worked on this subject.[2,5,11,12]

Concentrating our analysis on reset processes (among the many examples of RRAM devices published in the literature) there can be found linear and nonlinear reset I–V curves at low applied voltages (in both cases, once the reset voltage is achieved, the current usually drops off in an abrupt manner). In the linear case (considering the device in the LRS), the charge conduction in the conductive filaments shows an ohmic behaviour (in these conductive filaments drift is assumed to be the main transport mechanism). Nevertheless, the nonlinear case cannot be explained accounting only for ohmic behaviour, for this reason, we have to consider an additional charge transport approach in addition to those linked to the linear model. In examining this issue, we will come to giving the main keys of the charge transport properties and of the mechanisms controlling the dissolution and rupture of the conductive filaments that allow resistive switching in the devices under study here.

To do so, we will introduce substantial modifications on a previously developed RRAM simulator[9] and we will compare with experimental data (different reset I–V curves) obtained in long series of set/reset cycles. For circuit design and simulation purposes, understanding the reset processes is a key issue to deal with compact modeling and the parameter extraction needed to characterize a particular technology.[1,13]

The experimental data were obtained making use of $Ni/HfO_2/Si\text{-}n^+$ devices fabricated at the IMB-CNM lab in Barcelona. Similar devices were fabricated by other groups;[14] in particular, these latter authors proved with their analysis the presence of conductive filaments with a high concentration of Ni species. Taking into consideration results of other authors, concerning the metallic nature (connected with the active electrode) of the CFs in devices with a similar oxide (hafnium dioxide),[15,16] we assume a fully thermal dissolution process. In the simulation ground we used (and enhanced as it will be described in Sec. III) a tool[9,10] that includes the possibility of several coupled CFs where conduction takes place. This approach is consistent with the presence of a single filament with several branches (subfilaments), interlaced between them[17] or forming a tree structure.[15,18,19] The current, temperature, and temporal evolution of each CF are calculated self-consistently, including the

 © 2014 AIP Publishing LLC

series resistance at each CF (accounting for the Maxwell and the set-up resistances), heat exchange with the electrodes and the oxide, and the determination along each CF of the resistance per unit length (dependent on the temperature and on the CF shape and width).

The paper is organized as follows. In Sec. II, we give details of the fabricated devices and measurement set-up. The main features of the numerical simulator are given in Sec. III. In Sec. IV, we present the main results and the corresponding discussions; finally, the conclusions are drawn in Sec. V.

II. DEVICE FABRICATION AND MEASUREMENT SET-UP

The Ni/HfO_2/Si devices were fabricated on (100) n-type CZ silicon wafers with resistivity (0.007–0.013) Ω cm. The 20 nm-thick HfO_2 layers were deposited by atomic layer deposition at 200 °C using tetrakis (Dimethylamido)-hafnium (TDMAH) and H_2O as precursors, and N_2 as carrier and purge gas. After growth of the dielectric film, a high temperature anneal at 800 °C for 30 min in a N_2 ambient was performed. The top Ni electrode with a 200 nm thickness was deposited by magnetron sputtering. The area of the cells is $80 \times 80\ \mu m^2$. A schematic cross-section of the final device structure is shown in Fig. 1(a).

The I–V characteristics were measured using a HP-4155B semiconductor parameter analyzer. The voltage was applied to the top Ni electrode, while the Si substrate was grounded. In order to automatically perform successive I–V measurements and to smartly and dynamically detect the set and reset currents, the I–V meter was connected to the computer via GPIB (General Purpose Instrumentation Bus) and controlled using MATLAB. For this study, more than 3000 successive cycles were measured. Typical I–V characteristics during set and reset operations are shown in Fig. 1(b).

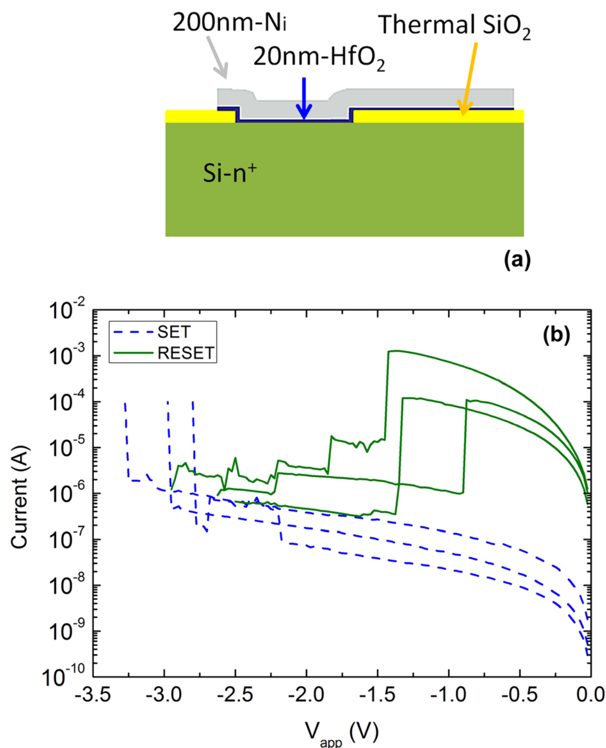

FIG. 1. (a) Cross section scheme of the Ni/HfO_2/Si-n^+ devices, (b) current-voltage characteristics during typical set and reset cycles. A current compliance of 100 μA has been employed.

III. SIMULATOR DESCRIPTION

The simulations shown in this work have been obtained with a new and enhanced version of the tool explained in Ref. 9. The RRAM simulator accounts for a structure with two different electrodes and an oxide in between, including the electrical and thermal properties of the materials. The structure simulated in Ref. 9 has been modified to study the devices sketched in Figure 1.

The basic scheme of the elements incorporated in the simulator is shown in Figure 2. As can be seen, an arbitrary number of CFs with different radii and shapes can be considered, including the series resistance (calculated summing the setup and Maxwell resistances of each CF). Taking into account the study of Ref. 14, where similar devices were used to those described in Sec. II, truncated-cone-shaped CFs are employed with the narrowest end placed at the interface of the dielectric and the n^+-Si layer.

In addition to what was shown in Ref. 9, in each of the branches in Figure 2 (corresponding each one to a different CF) a module is included to represent the presence of a CF constriction (this filamentary path is assumed to be placed at the dielectric-n^+Si interface) that is modeled accordingly to the Quantum Point Contact (QPC) theory. To analyze the charge transport at this CF narrowing we have followed Refs.

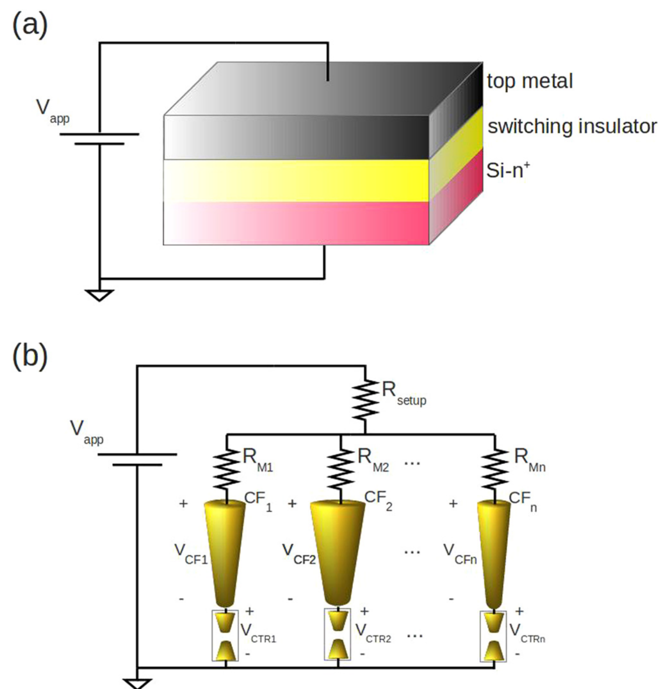

FIG. 2. Schematic of the structure considered in this study (a), and the electrical equivalent circuit considered for the simulator development (b). R_{setup} is the resistance of the measurement setup and in-chip wires, and CF_i is the *ith* conductive filament across the insulator, while R_{Mi} are the Maxwell's resistances. Each CF is independently modelled by a different conductive path (with cylindrical symmetry and a truncated cone shape) and a filamentary path at the CF end placed at the dielectric-n^+Si interface; in this latter element the QPC model is employed.

20 and 21 (in this constriction, the first quantized sub-band behaves as a potential barrier for the transit of electrons).

We have followed the assumptions described in Refs. 20 and 21 to obtain an analytical expression for the current at the CF (Eq. (1)), where a parabolic potential barrier is considered (see that we use the voltage drop at the constriction because we accurately calculate the other resistive elements within the real structure and solve self-consistently the temporal, thermal and electric behaviour of the device)

$$I = \frac{2eN}{h}\left\{ eV_{CTR} + \frac{1}{\alpha} Ln\left[\frac{1+\exp\{\alpha[\Phi - \beta eV_{CTR}]\}}{1+\exp\{\alpha[\Phi + (1-\beta)eV_{CTR}]\}} \right] \right\}. \quad (1)$$

For this model (the Landauer's formalism for 1D quantum conductors and the zero-temperature limit was employed[20,21]), Φ is assumed to be the potential barrier height measured with respect to the Fermi level, α is a parameter linked to the potential barrier thickness at the Fermi level, V_{CTR} is the voltage which is assumed to drop at both ends of the CF constriction (in a fraction of β and (1-β) at each extreme, as suggested in Refs. 22 and 23; this latter assumption is reasonable since there are different materials at both ends of the filamentary path), e is the elementary electron charge, I is the CF current, and N is the number of active channels in the CF.[21,23]

In addition to the magnitudes described above, a series resistance was considered in Ref. 21; however, as explained above, in our case, we calculate this resistance adding the contributions of the setup resistance, Maxwell resistance, and the resistance of the "thick" part of the conductive filament (from the Ni electrode to the CF narrowing at the dielectric-n^+Si interface), for each branch. In this respect, within the self-consistent scheme that we explained above, V_{CTR} can be calculated for each CF, corresponding to a different branch in Figure 2, as follows:

$$V_{CTR,i} = V_{app} - I_{total} \cdot R_{setup} - I_i \cdot (R_{M,i} + R_{CF,i}), \quad (2)$$

where $R_{M,i}$, $R_{CF,i}$, and I_i stand for the Maxwell resistance, the CF resistance, and the CF current of i-branch (corresponding to CF (i)) as sketched in Figure 2. I_{total} is calculated as the sum of the currents in all the CFs considered in a particular device. It should be noted that in this way, we can calculate the voltage outside the barrier and take into account for the calculation of the tunneling current only the voltage truly applied in the constriction, which results in a better fit of the experimental curves as suggested in Ref. 22.

The length of the CF narrowing is represented by the t_B parameter of the model (width of the barrier at the reference energy E = 0). It was estimated in Ref. 20 for the devices they analysed; the following values were found, $1.1\,\text{nm} < t_B < 2.3\,\text{nm}$, for α and Φ values of their fitting according to

$$\alpha = t_B \pi^2 h^{-1} \sqrt{\frac{2m^*}{\Phi}}, \quad (3)$$

where m^* is the electron effective mass in the constriction. In our case, we used α and Φ values of the same order and, therefore, similar values of t_B would be expected, which are less than 10% of the CF length (even assuming a straight CF crossing the dielectric in a perpendicular direction to the electrodes plane (in our devices, $t_{ox} = 20\,\text{nm}$)).

Using α, β, and N as fitting parameters for each curve, the narrowest end of each CF can be modeled. Furthermore, we can approximately calculate its radius. To do so, we estimate the number of Ni ions that can be ideally placed in a circle (the narrowest end of a truncated-cone-shaped CF), and using N (number of active channel in the CF, Eq. (1)) as this number, the radius of the CF narrower part is calculated. The radius of the other end allows the fitting of the I–V curve as well as the V_{reset} voltage for a particular reset cycle. As will be shown below, the inclusion of both transport components of the CF resistance (described by means of a classical –ohmic regime- and quantum –tunnelling regime-) are needed to correctly simulate the devices we are considering. Several CFs are considered in the same device if the I–V curve presents several current steps following Ref. 9.

Once the simulation starts, the radius in each position of the CF is determined by the temporal evolution of the diffusion processes of the metal atoms that form the CF.[9] The temperature along the CFs is calculated by solving the heat equation, where the heat dissipation to the electrodes and the surrounding oxide is considered. The current is obtained making use of Eqs. (1) and (2) and by calculating the CF resistances, accounting for the evolution of the conductivity with the temperature, and the CFs shape at each grid point between the electrodes. The total electric current, temperature, and time evolution of all the CFs are solved self-consistently for each applied voltage till the high resistance state is achieved. The set of constants employed in the simulator, to fit the measured curves, is given below in Table I.

IV. RESULTS AND DISCUSSION

We have used our simulator to reproduce the measurements obtained for the devices described in Sec. II (see Figure 3). We have selected several reset I–V curves with just one deep current step (Figure 3(a)), these cycles were reproduced making use of a single CF. In Figure 3(b) curves with several current steps were plotted, in these case several CFs were employed following previous results reported in Ref. 9, 4 CFs for cycles 1001 and 211, and 2 CFs for cycle 151.

As explained in Sec. III, for the devices under study, truncated-cone-shaped CFs were employed.[14] In this respect, and following the notation developed in Ref. 9, the maximum radii of the CFs used (r_{CFmax}) were given in Figure 3,

TABLE I. Physical parameters used in the simulations.

k_{diff}	$5 \times 10^8\,\text{s}^{-1}$
α_T	$5 \times 10^{-3}\,\text{K}^{-1}$
E_a	1.2 eV
h	$4 \times 10^{10}\,\text{W K}^{-1}\,\text{m}^{-2}$
k_{th}	$3\,\text{W K}^{-1}\,\text{m}^{-1}$
σ_{ox}	$1.25\,\Omega^{-1}\,\text{m}^{-1}$
σ_{CF0}	$3 \times 10^5\,\Omega^{-1}\,\text{m}^{-1}$
σ_{Ni}	$8.33 \times 10^6\,\Omega^{-1}\,\text{m}^{-1}$
σ_{Sin+}	$1 \times 10^4\,\Omega^{-1}\,\text{m}^{-1}$

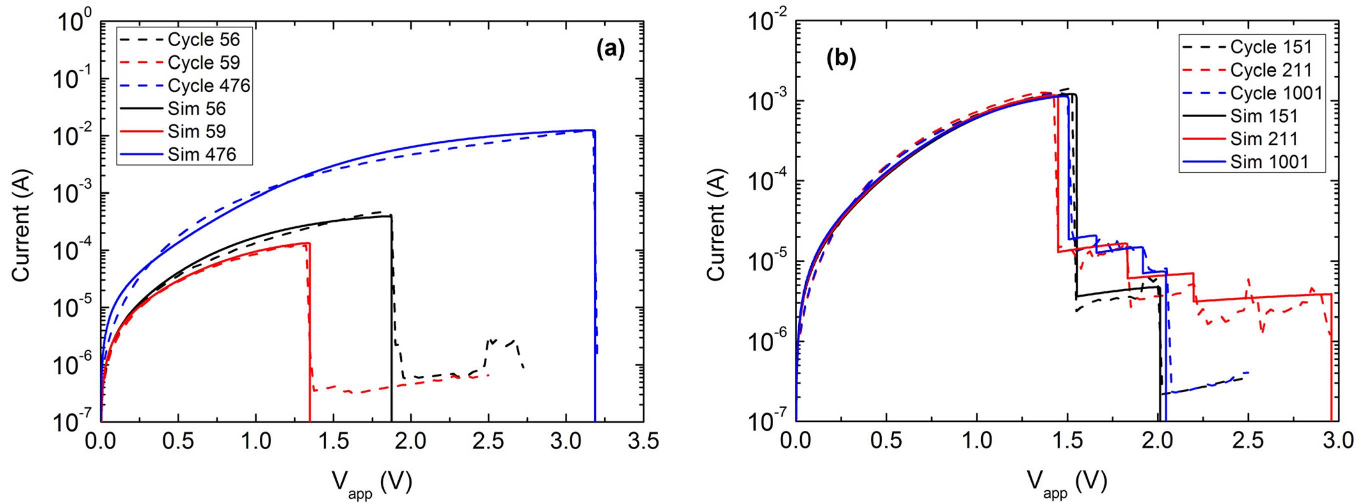

FIG. 3. RRAM current versus applied voltage. The experimental measurements of the devices described in Sec. II are shown in dashed lines and the simulation results are plotted in solid lines. Truncated-cone-shaped CFs were used, with the following sizes (r_{CFmax} accounts for the maximum radius of the CF and C_{CF0} is the fraction of this maximum radius in the narrowest part of the truncated cone).(a) A single CF was considered in all cases, at the beginning of the simulation the CF features were the following: ($r_{CFmax} = 9$ nm, $C_{CF0} = 17\%$) for Sim 56, ($r_{CFmax} = 12$ nm, $C_{CF0} = 6\%$) for Sim 59, and ($r_{CFmax} = 27$ nm, $C_{CF0} = 60\%$) for Sim 476; (b) Several CFs were employed here, for simulation 151, the conductive path consists of two subfilaments with the following characteristics: (CF_1: $r_{CFmax1} = 30$ nm, $C_{CF0} = 9{,}5\%$; CF_2: $r_{CFmax2} = 1.5$ nm, $C_{CF0} = 6\%$); similarly, for simulation 211 we used the following configuration (CF_1: $r_{CFmax1} = 38$ nm, $C_{CF0} = 7\%$; CF_2: $r_{CFmax2} = 3$ nm, $C_{CF0} = 5\%$; CF_3: $r_{CFmax3} = 0.9$ nm, $C_{CF0} = 8.89\%$; CF_4: $r_{CFmax3} = 0.58$ nm, $C_{CF0} = 13.79\%$) and for simulation 1001 we used the following configuration (CF_1: $r_{CFmax1} = 30$ nm, $C_{CF0} = 9\%$; CF_2: $r_{CFmax2} = 3$ nm, $C_{CF0} = 4.3\%$; CF_3: $r_{CFmax3} = 2.5$ nm, $C_{CF0} = 5\%$; CF_4: $r_{CFmax3} = 2$ nm, $C_{CF0} = 6\%$).

the reduction of the narrowest part of the CF is described by means of the C_{CF0} parameter. $C_{CF}(z)$ shows the ratio of the CF radius that is formed at a given vertical position (z) assuming a certain CF shape (a cylinder or a truncated cone) with a given maximum radius. In this way we describe the evolution of the CFs thickness along the device, the radius of the CF is calculated as $r_{CF}(z) = r_{CFmax} \cdot C_{CF}(z)$. In truncated-cone-shaped CFs, the C_{CF0} parameters account for the radius of the narrowest part of the CF; in all the cases, the corresponding area is above the area related to a single line of Ni atoms (the ionic Ni radius has been considered here), obviously $N = 1$ has to be used in Eq. (1) if the latter case is assumed.

Along with the parameters that describe the CFs we have included those that account for the QPC model. In this respect, taking into consideration that each CF is formed in a different manner in each set/reset cycle, these parameters have to be fitted to reproduce the experimental data. Four parameters can be used in Eq. (1); two of them were the same for all the simulations performed here ($\Phi = 1.2$ eV and $\beta = 0.9$), we changed N and α for each CF (e.g., $N = 276$ and $\alpha = 5.5$ for cycle 56 and $N = 56$ and $\alpha = 4.1$ for cycle 59; since the CFs are changed from cycle to cycle, new α and N parameters would be needed). As can be seen, the low current part of the reset curve is correctly reproduced for all the cases considered, in this regime the correct modeling of the nonlinear behaviour is of most importance.

We can assess the value of parameter t_B (Eq. (2)). In this respect, all the values of t_B for the devices analyzed here are within the following interval [0.51 nm, 1.13 nm], considering a dielectric effective mass of $0.44m_0$. This means that the approximate CF narrowing length is less than a 5% of the total CF length in our study.

A simulation of a single CF device I–V curve is shown in Figure 4(a). The corresponding thick part of the CF resistance (R_{CF}) and the resistance connected with the constriction (R_{QPC}) at the oxide-n^+ Si interface (the latter described by means of the QPC model) are shown in Figure 4(b). As can be seen, the R_{QPC} is higher at low applied voltages in comparison with R_{CF}. In this respect, at low applied voltages, the device current is controlled almost exclusively by the CF narrowing limited current. However, as the applied voltage increases, R_{QPC} drops off and consequently the role of the constriction in determining the current is less important and might be even irrelevant. See that once the reset voltage is achieved, both resistance components diverge due to the CF rupture. A HRS is achieved after the reset process is complete.

The description of this process from the thermal viewpoint is sketched in Figure 4(c). The temperature along the CF is plotted for the voltage sweep employed in Figure 4(a). See that at the reset voltage the CF temperature peaks (this sudden rise is reasonable within the self-accelerated process that takes place when the CF is ruptured[9]).

In Figure 5(a), two I–V curves are simulated for identical RRAM devices with different values of the α parameter of Eq. (1). See the influence of this choice on the non-linear characteristics of the current curves at low voltages and also on the determination of the reset voltage.

R_{CF} and R_{QPC} for the curves shown in Figure 5(a) are given in Figure 5(b). A sudden rise is again seen when the CF is broken for both α values. However, important differences in the relative values of the resistance components can be seen for the two α values selected. The role of the nonlinear component is higher for the higher α parameter (see Eq. (2), this fact implies a thicker potential barrier (t_B)).

FIG. 4. (a) Simulated RRAM current versus applied voltage (the corresponding simulation time is also shown, a ramp of 0.1 V/s was used) for a device with a single CF. (b) Evolution of R_{CF} and R_{QPC} versus applied voltage. (c) CF temperature along the oxide for all the applied voltages considered in the I–V reset curve of (a).

Finally, we have compared a set of experimental reset current and voltage values for a large sample of I–V curves with simulations (Figure 6). See that the model reproduces accurately different zones of this plot, these zones represent configurations where one of the different components of the device resistance has more influence over the others (we are considering R_{CF} and R_{QPC} and R_M in our analysis).[9]

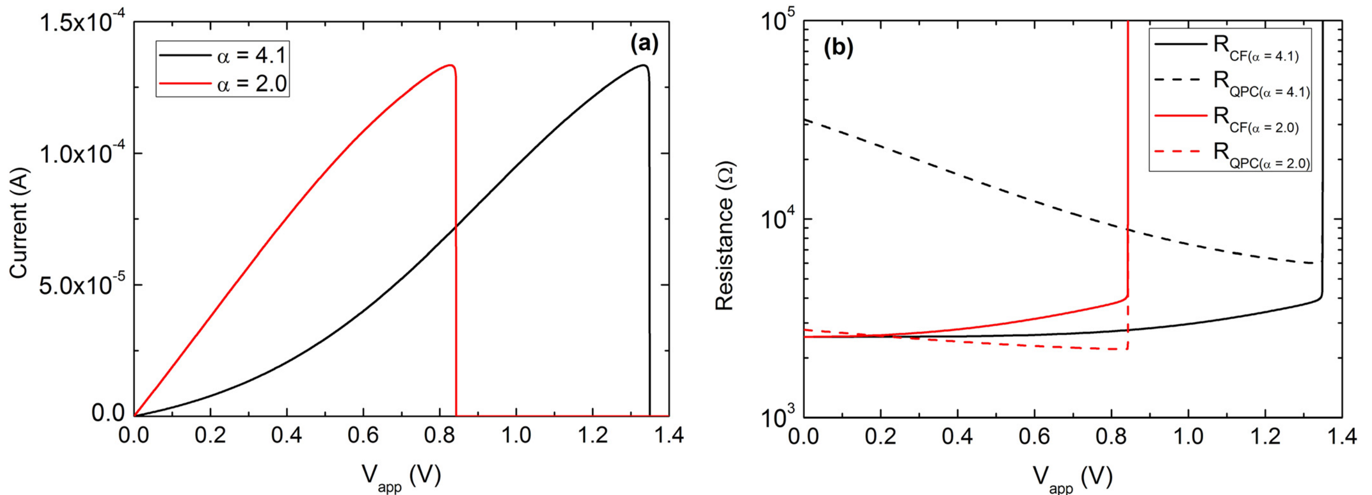

FIG. 5. (a) Simulated RRAM current versus applied voltage for a device with a single CF (two different α parameters are employed in Eq. (1)). (b) Evolution of R_{CF} and R_{QPC} versus applied voltage for the cases considered in (a).

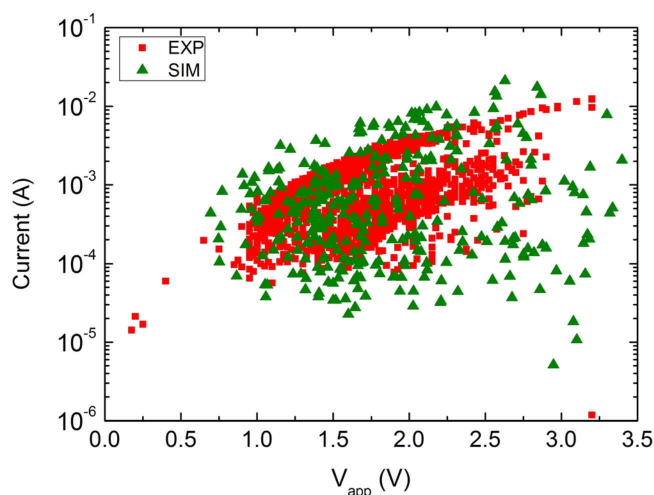

FIG. 6. RRAM current versus reset voltage (V_{app}). Simulated data for a set of devices whose features have been generated randomly (the number of CFs and their radius, assuming truncated cone shapes) and experimental data from the devices described in Sec. II are shown together for comparison.

V. CONCLUSIONS

A simulator tool to describe reset processes in RRAM devices has been developed, including quantum effects. Experimental measurements of RRAMs based on $Ni/HfO_2/Si\text{-}n^+$ structures have been reproduced for devices with a different number of conductive filaments and for all the operation regimes considered. The simulator includes the electrical and thermal description of the devices and the temporal evolution of the conductive filaments, the series resistance is also included. Both the ohmic and tunneling based conduction regimes are considered; their contribution and the operation regimes where one or the other are dominant.

ACKNOWLEDGMENTS

UGR authors thank the support of Junta de Andalucía under project FQM.1861 and the Spanish Ministerio de Economía y Competitividad under Contract No. TEC2011-28660 (partially supported by the EU under the FEDER program). UAB authors acknowledge funding by the Spanish Ministerio de Economía y Competitividad under Contract No. TEC2012-32305 (partially supported by the EU under the FEDER program), the DURSI of the Generalitat de Catalunya under Contract No. 2009SGR78. J. Suñé also thanks the funding support of the ICREA ACADEMIA award. IMB-CNM authors thank the support of the Spanish Ministry of Economy and Competitiveness under Project No. TEC2011-27292-C02-02, and the DURSI of the Generalitat de Catalunya through Project No. 2009SGR228. M. B. Gonzalez also thanks CSIC and ESF for a JAE-DOC contract.

[1]See http://public.itrs.net for the international technology roadmap for semiconductors, ed. 2011 and 2012 update.

[2]S. Long, C. Cagli, D. Ielmini, M. Liu, and J. Suñé, "Analysis and modeling of resistive switching statistics," J. Appl. Phys. **111**, 074508 (2012).

[3]H. S. P. Wong, H. Y. Lee, S. Yu, Y.-S. Chen, Y. Wu, P.-S. Chen, B. Lee, F. T. Chen, and M.-J. Tsai. "Metal-oxide RRAM," Proc. IEEE **100**(6), 1951–1970 (2012).

[4]I. G. Baek, D. C. Kim, M. J. Lee, H.-J. Kim, E. K. Yim, M. S. Lee, J. E. Lee, S. E. Ahn, S. Seo, J. H. Lee, J. C. Park, Y. K. Cha, S. O. Park, H. S. Kim, I. K. Yoo, U-In Chung, J. T. Moon, and B. I. Ryu, "Multi-layer cross-point binary oxide resistive memory (OxRRAM) for post-NAND storage application," IEDM Tech. Dig. **2005**, 750–753.

[5]U. Russo, C. Cagli, and A.-L. Lacaita, "Self-accelerated thermal dissolution model for reset programming in unipolar resistive-switching memory (RRAM) devices," IEEE Trans. Electron Dev. **56**(2), 193–200 (2009).

[6]U. Russo, C. Cagli, and A.-L. Lacaita, "Filament conduction and reset mechanism in NiO-based resistive-switching memory (RRAM) devices," IEEE Trans. Electron Dev. **56**(2), 186–192 (2009).

[7]S. Long, X. Lian, T. Ye, C. Cagli, L. Perniola, E. Miranda, M. Liu, and J. Suñé, "Cycle-to-cycle intrinsic RESET statistics in HfO_2-based unipolar RRAM devices," IEEE Electron Dev. Lett. **34**(5), 623–625 (2013).

[8]S. Long, C. Cagli, J. Bucley, X. Lian, M. Liu, and J. Suñé, "Voltage and power-controlled regimes in the progressive unipolar RESET transition of HfO_2-based RRAM," Sci. Rep. **3**, 2929 (2013).

[9]M. A. Villena, F. Jimenez-Molinos, J. B. Roldán, J. Suñé, S. Long, X. Lian, F. Gámiz, and M. Liu, "An in-depth simulation study of thermal reset transitions in RRAM," J. Appl. Phys. **114**, 144505 (2013).

[10]M. A. Villena, F. Jiménez-Molinos, J. B. Roldán, J. Suñé, S. Long, E. Miranda, and M. Liu, "A comprehensive analysis on progressive reset transitions in RRAMs," J. Phys. D: Appl. Phys. **47**, 205102 (2014).

[11]D. Ielmini, F. Nardi, and C. Cagli, "Physical models of size-dependent nanofilament formation and rupture in NiO resistive switching memories," Nanotechnology **22**, 254022 (2011).

[12]M. Bocquet, D. Deleruyelle, C. Muller, and J.-M. Portal. "Self-consistent physical modeling of set/reset operations in unipolar resistive-switching memories," Appl. Phys. Lett. **98**, 263507 (2011).

[13]J. Wu, J. Cao, W. Han, A. Janotti, and H. C. Kim, *Functional Metal Oxide Nanostructures* (Springer-Verlag, 2012).

[14]X. Wu, D. Cha, M. Bosman, N. Raghavan, D. B. Migas, V. E. Borisenko, X. Zhang, K. Li, and K. Pey, "Intrinsic nanofilamentation in resistive switching," J. Appl. Phys. **113**, 114503 (2013).

[15]L. M. Yang, Y. L. Song, Y. Liu, Y. L. Wang, X. P. Tian, M. Wang, Y. Y. Lin, R. Huang, Q. T. Zou, and J. G. Wu, "Linear scaling of reset current down to 22-nm node for a novel Cu_xSi_yO RRAM," IEEE Electron Dev. Lett. **33**, 89 (2012).

[16]X. Yang, S. Long, K. Zhang, X. Liu, X. Lian, Q. Liu, H. Lv, M. Wang, H. Xie, H. Sun, P. Sun, J. Suñé, and M. Liu, "Investigation on the RESET switching mechanism of bipolar $Cu/HfO_2/Pt$ RRAM devices with a statistical methodology," J. Phys. D: Appl. Phys. **46**, 245107 (2013).

[17]S. B. Lee, S. C. Chae, S. H. Chang, L. S. Lee, S. Seo, B. Kahng, and T. W. Noh, "Scaling behaviors of reset voltages and currents in unipolar resistance switching," Appl. Phys. Lett. **93**, 212105 (2008).

[18]S. C. Chae, J. S. Lee, S. Kim, S. B. Lee, S. H. Chang, C. Liu, B. Kahng, H. Shin, D.-W. Kim, C. U. Jung, S. Seo, M.-J. Lee, and T. W. Noh. "Random circuit breaker network model for unipolar resistance switching," Adv. Mater. **20**, 1154 (2008.)

[19]J. S. Lee, S. B. Lee, S. H. Chang, L. G. Gao, B. S. Kang, M. J. Lee, C. J. Kim, T. W. Noh, and B. Kahng. "Scaling theory for unipolar resistance switching," Phys. Rev. Lett. **105**, 205701 (2010).

[20]E. Miranda, C. Walczyk, C. Wenger, and T. Schroeder, "Model for the resistive switching effect in HfO_2 MIM structures based on the transmission properties of narrow constrictions," IEEE Electron Device Lett. **31**, 609 (2010).

[21]L. M. Procel, L. Trojman, J. Moreno, F. Crupi, V. Maccaronio, R. Degraeve, L. Goux, and E. Simoen, "Experimental evidence of the quantum point contact theory in the conduction mechanism of bipolar HfO_2-based resistive random access memories," J. Appl. Phys. **114**, 074509 (2013).

[22]E. Miranda and J. Suñé,"Analytic modeling of leakage current through multiple breakdown paths in SiO_2 films," in *Proceedings of IEEE International Reliability Physics Symposium* (2001), p. 367.

[23]X. Lian, S. Long, C. Cagli, J. Buckley, E. Miranda, M. Liu, and J. Suñé, "Quantum Point Contact model of filamentary conduction in resistive switching devices," ULIS **2012**, 101–104.

Journal of Applied Physics is copyrighted by the American Institute of Physics (AIP). Redistribution of journal material is subject to the AIP online journal license and/or AIP copyright. For more information, see http://ojps.aip.org/japo/japcr/jsp